Protons in Near Earth Orbit

The AMS Collaboration

Abstract

The proton spectrum in the kinetic energy range 0.1 to 200 GeV was measured by the Alpha Magnetic Spectrometer (AMS) during space shuttle flight STS–91 at an altitude of 380 km. Above the geomagnetic cutoff the observed spectrum is parameterized by a power law. Below the geomagnetic cutoff a substantial second spectrum was observed concentrated at equatorial latitudes with a flux $\sim 70\,\mathrm{m}^{-2}\mathrm{sec}^{-1}\mathrm{sr}^{-1}$. Most of these second spectrum protons follow a complicated trajectory and originate from a restricted geographic region.

Submitted to *Phys. Lett. B*

Introduction

Protons are the most abundant charged particles in space. The study of cosmic ray protons improves the understanding of the interstellar propagation and acceleration of cosmic rays.

There are three distinct regions in space where protons have been studied by different means:

- The altitudes of 30–40 km above the Earth's surface. This region has been studied with balloons for several decades. Balloon experiments have made important contributions to the understanding of the primary cosmic ray spectrum of protrons and the behavior of atmospheric secondary particles in the upper layer of the atmosphere.

- The inner and outer radiation belts, which extend from altitudes of about 1000 km up to the boundary of the magnetosphere. Small size detectors on satellites have been sufficient to study the high intensities in the radiation belts.

- A region intermediate between the top of the atmosphere and the inner radiation belt. The radiation levels are normally not very high, so satellite-based detectors used so far, *i.e.* before AMS, have not been sensitive enough to systematically study the proton spectrum in this region over a broad energy range.

Reference [**?**] includes some of the previous studies. The primary feature in the proton spectrum observed near Earth is a low energy drop off in the flux, known as the geomagnetic cutoff. This cutoff occurs at kinetic energies ranging from ~10 MeV to ~10 GeV depending on the latitude and longitude. Above cutoff, from ~10 to ~100 GeV, numerous measurements indicate the spectrum falls off according to a power law.

The Alpha Magnetic Spectrometer (AMS) [**?**] is a high energy physics experiment scheduled for installation on the International Space Station. In preparation for this long duration mission, AMS flew a precursor mission on board the space shuttle Discovery during flight STS–91 in June 1998. In this report we use the data collected during the flight to study the cosmic ray proton spectrum from kinetic energies of 0.1 to 200 GeV, taking advantage of the large acceptance, the accurate momentum resolution, the precise trajectory reconstruction and the good particle identification capabilities of AMS.

The high statistics (~ 10^7) available allow the variation of the spectrum with position to be measured both above and below the geomagnetic cutoff. Because the incident particle direction and momentum were accurately measured in AMS, it is possible to investigate the origin of protons below cutoff by tracking them in the Earth's magnetic field.

The AMS Detector

The major elements of AMS as flown on STS–91 consisted of a permanent magnet, a tracker, time of flight hodoscopes, a Cerenkov counter and anticoincidence counters [**?**]. The permanent magnet had the shape of a cylindrical shell with inner diameter 1.1 m, length 0.8 m and provided a central dipole field of 0.14 Tesla across the magnet bore and an analysing power, BL^2, of 0.14 Tm^2 parallel to the magnet, or z–, axis. The six layers of double sided silicon tracker were arrayed transverse to the magnet axis. The outer layers were just outside the magnet cylinder. The tracker measured the trajectory of relativistic singly charged particles with an accuracy of 20 microns in the bending coordinate and 33 microns in the non-bending coordinate, as well as providing multiple measurements of the energy loss. The time of flight system had two planes at each end of the magnet, covering the

outer tracker layers. Together the four planes measured singly charged particle transit times with an accuracy of 120 psec and also yielded multiple energy loss measurements. The Aerogel Cerenkov counter ($n = 1.035$) was used to make independent velocity measurements to separate low energy protons from pions and electrons. A layer of anticoincidence scintillation counters lined the inner surface of the magnet. Low energy particles were absorbed by thin carbon fiber shields. In flight the AMS positive z–axis pointed out of the shuttle payload bay.

For this study the acceptance was restricted to events with an incident angle within 32° of the positive z–axis of AMS and data from two periods are included. In the first period the z–axis was pointing within 1° of the zenith. Events from this period are referred to as "downward" going. In the second period the z–axis pointing was within 1° of the nadir. Data from this period are referred to as "upward" going. The orbital inclination was 51.7° and the geodetic altitude during these two periods ranged from 350 to 390 km. Data taken while orbiting in or near the South Atlantic Anomaly were excluded.

The response of the detector was simulated using the AMS detector simulation program, based on the GEANT package [**?**]. The effects of energy loss, multiple scattering, interactions, decays and the measured detector efficiency and resolution were included.

The AMS detector was extensively calibrated at two accelerators: at GSI, Darmstadt, with helium and carbon beams at 600 incident angles and locations and 10^7 events, and at the CERN proton-synchrotron in the energy region of 2 to 14 GeV, with 1200 incident angles and locations and 10^8 events. This ensured that the performance of the detector and the analysis procedure were thoroughly understood.

Analysis

Reconstruction of the incident particle type, energy and direction started with a track finding procedure which included cluster finding, cluster coordinate transformation and pattern recognition. The track was then fit using two independent algorithms [**?**, **?**]. For a track to be accepted the fit was required to include at least 4 hits in the bending plane and at least 3 hits in the non-bending plane.

The track was then extrapolated to each time of flight plane and matched with the nearest hit if it was within 60 mm. Matched hits were required in at least three of the four time of flight planes. The velocity, $\beta = v/c$, was then obtained using this time of flight information and the trajectory. For events which passed through the Cerenkov counter sensitive volume an independent velocity measurement, β_C, was also determined. To obtain the magnitude of the particle charge, $|Z|$, a set of reference distributions of energy losses in both the time of flight and the tracker layers were derived from calibration measurements made at the CERN test beam interpolated via the Monte Carlo method. For each event these references were fit to the measured energy losses using a maximum likelihood method. The track parameters were then refit with the measured β and Z and the particle type determined from the resultant Z, β, β_C and rigidity, $R = pc/|Z|e$ (GV).

As protons and helium nuclei are the dominant components in cosmic rays, after selecting events with $Z = +1$ the proton sample has only minor backgrounds which consist of charged pions and deuterons. The estimated fraction of charged pions, which are produced in the top part of AMS, with energy below 0.5 GeV is 1 %. Above this energy the fraction decreases rapidly with increasing energy. The deuteron abundance in cosmic rays above the geomagnetic cutoff is about 2 %. To remove low energy charged pions and deuterons the measured mass was required to be within 3 standard deviations of the proton mass. This rejected about 3 % of the events while reducing the background contamination to negligible levels over all energies.

To determine the differential proton fluxes from the measured counting rates requires the acceptance to be known as a function of the proton momentum and direction. Protons with different momenta and directions were generated via the Monte Carlo method, passed through the AMS detector simulation program and accepted if the trigger and reconstruction requirements were satisfied as for the data. The acceptance was found to be $0.15\,m^2sr$ on average, varying from 0.3 to $0.03\,m^2sr$ with incident angle and location and only weakly momentum dependent. These acceptances were then corrected following an analysis of unbiased trigger events. The corrections to the central value are shown in Table 1 together with their contribution to the total systematic error of 5 %.

Correction	Amount	Uncertainty
Trigger:		
4–Fold Coincidence	−3	1.5
Time of Flight Pattern	−4	2
Tracker Hits	−2	1
Anticoincidence	0	1
Analysis:		
Track and Velocity Fit	−2	1.5
Particle Interactions	+1	1.5
Proton Selection	−2	2
Monte Carlo Statistics	0	2
Differential Acceptance Binning	0	2
Total	**−12**	**5**

Table 1: Acceptance corrections and their systematic uncertainties, in percent

To obtain the incident differential spectrum from the measured spectrum, the effect of the detector resolution was unfolded using resolution functions obtained from the simulation. These functions were checked at several energy points by test beam measurements. The data were unfolded using a method based on Bayes' theorem [**?**, **?**], which used an iterative procedure (and not a "regularized unfolding") to overcome instability of the matrix inversion due to negative terms. Fig. 1 compares the differential proton spectrum before and after unfolding in the geomagnetic equatorial region, defined below.

Results and Interpretation

The differential spectra in terms of kinetic energy for downward and upward going protons integrated over incident angles within 32° of the AMS z–axis, which was within 1° of the zenith or nadir, are presented in Fig. 2 and Tables 2–4. The results have been separated according to the absolute value of the corrected geomagnetic latitude [**?**], Θ_M (radians), at which they were observed. Figs. 2a, b and c clearly show the effect of the geomagnetic cutoff and the decrease in this cutoff with increasing Θ_M. The spectra above and below cutoff differ. The spectrum above cutoff is refered to as the "primary" spectrum and below cutoff as the "second" spectrum.

I. Properties of the Primary Spectrum

The primary proton spectrum may be parameterized by a power law in rigidity, $\Phi_0 \times R^{-\gamma}$. Fitting [**?**] the measured spectrum over the rigidity range $10 < R < 200$ GV, *i.e.* well above cutoff, yields:

$$\gamma = 2.79 \pm 0.012\,(\text{fit}) \pm 0.019\,(\text{sys}),$$

$$\Phi_0 = 16.9 \pm 0.2\,(\text{fit}) \pm 1.3\,(\text{sys}) \pm 1.5\,(\gamma)\ \frac{\text{GV}^{2.79}}{\text{m}^2\text{sec sr MV}}\ .$$

The systematic uncertainty in γ was estimated from the uncertainty in the acceptance (0.006), the dependence of the resolution function on the particle direction and track length within one sigma (0.015), variation of the tracker bending coordinate resolution by $\pm$ 4 microns (0.005) and variation of the selection criteria (0.010). The third uncertainty quoted for Φ_0 reflects the systematic uncertainty in γ.

II. Properties of the Second Spectrum

As shown in Figs. 2a, b, c, a substantial second spectrum of downward going protons is observed for all but the highest geomagnetic latitudes. Figs. 2d, e, f show that a substantial second spectrum of upward going protons is also observed for all geomagnetic latitudes. The upward and downward going protons of the second spectrum have the following unique properties:

(i) At geomagnetic equatorial latitudes, $\Theta_M < 0.2$, this spectrum extends from the lowest measured energy, 0.1 GeV, to ~6 GeV with a flux ~70 $m^{-2}sec^{-1}sr^{-1}$.

(ii) As seen in Figs. 2a, d, the second spectrum has a distinct structure near the geomagnetic equator: a change in geomagnetic latitude from 0 to 0.3 causes the proton flux to drop by a factor of 2 to 3 depending on the energy.

(iii) Over the much wider interval $0.3 < \Theta_M < 0.8$, the flux is nearly constant.

(iv) In the range $0 \leq \Theta_M < 0.8$, detailed comparison in different latitude bands (Fig. 3) indicates that the upward and downward fluxes are nearly identical, agreeing within 1 %.

(v) At polar latitudes, $\Theta_M > 1.0$, the downward second spectrum (Fig. 2c) is gradually obscured by the primary spectrum, whereas the second spectrum of upward going protons (Fig. 2f) is clearly observed.

To understand the origin of the second spectrum, we traced [**?**] back 10^5 protons from their measured incident angle, location and momentum, through the geomagnetic field [**?**] for 10 sec flight time or until they impinged on the top of the atmosphere at an altitude of 40 km, which was taken to be the point of origin. All second spectrum protons were found to originate in the atmosphere, except for few percent of the total detected near the South Atlantic Anomaly (SAA). These had closed trajectories and hence may have been circulating for a very long time and it is obviously difficult to trace back to thier origin. This type of trajectory was only observed near the SAA, clearly influenced by the inner radiation belt. To avoid confusion data taken in the SAA region were excluded though the rest of the protons detected near the SAA had characteristics as the rest of the sample. Defining the flight time as the interval between production and detection, Fig. 4 shows the distribution of momentum versus flight time of the remaining protons.

As seen in Fig. 4, the trajectory tracing shows that about 30 % of the detected protons flew for less than 0.3 sec before detection. The origin of these "short–lived" protons is distributed uniformly around the globe, see Fig. 5a, the apparent structure reflecting the orbits of the space shuttle. In contrast, Fig. 5b shows that the remaining 70 % of protons with flight times greater than 0.3 sec, classified as "long–lived", originate from a geographically restricted zone. Fig. 6 shows the strongly peaked distribution of the point of origin of these long–lived protons in geomagnetic coordinates. Though data is presented only for protons detected at $\Theta_M < 0.3$, these general features hold true up to $\Theta_M \sim 0.7$. Fig. 7 shows the distribution of the number of geomagnetic equator crossings for long–lived and short–lived protons. About 15 % of all the second spectrum protons were detected on their first bounce over the geomagnetic equator.

The measurements by AMS in near Earth orbit (at 380 km from the Earth's surface), between the atmosphere and the radiation belt, show that the particles in this region follow a complicated path in the Earth's magnetic field. This behavior is different from that extrapolated from satellite observations in the radiation belts, where the protons bounce across the equator for a much longer time. It is also different from that extrapolated from balloon observations in the upper layer of the atmosphere, where the protons typically cross the equator once. A striking feature of the second spectrum is that most of the protons originate from a restricted geographic region.

Acknowledgements

The support of INFN, Italy, ETH–Zürich, the University of Geneva, the Chinese Academy of Sciences, Academia Sinica and National Central University, Taiwan, the RWTH–Aachen, Germany, the University of Turku, the University of Technology of Helsinki, Finland, the U.S. DOE and M.I.T., CIEMAT, Spain, LIP, Portugal and IN2P3, France, is gratefully acknowledged.

We thank Professors S. Ahlen, C. Canizares, A. De Rujula, J. Ellis, A. Guth, M. Jacob, L. Maiani, R. Mewaldt, R. Orava, J. F. Ormes and M. Salamon for helping us to initiate this experiment.

The success of the first AMS mission is due to many individuals and organizations outside of the collaboration. The support of NASA was vital in the inception, development and operation of the experiment. The dedication of Douglas P. Blanchard, Mark J. Sistilli, James R. Bates, Kenneth Bollweg and the NASA and Lockheed–Martin Mission Management team, the support of the Max–Plank Institute for Extraterrestrial Physics, the support of the space agencies from Germany (DLR), Italy (ASI), France (CNES) and China and the support of CSIST, Taiwan, made it possible to complete this experiment on time.

The support of CERN and GSI–Darmstadt, particularly of Professor Hans Specht and Dr. Reinhard Simon made it possible for us to calibrate the detector after the shuttle returned from orbit.

The back tracing was made possible by the work of Professors E. Flückiger, D. F. Smart and M. A. Shea.

We are most grateful to the STS–91 astronauts, particularly to Dr. Franklin Chang–Diaz who provided vital help to AMS during the flight.

The AMS Collaboration

J.Alcaraz[y], D.Alvisi[j], B.Alpat[ac], G.Ambrosi[r], H.Anderhub[ag], L.Ao[g], A.Arefiev[ab], P.Azzarello[r], E.Babucci[ac], L.Baldini[j,l], M.Basile[j], D.Barancourt[s], F.Barao[w,v], G.Barbier[s], G.Barreira[w], R.Battiston[ac], R.Becker[l], U.Becker[l], L.Bellagamba[j], P.Béné[r], J.Berdugo[y], P.Berges[l], B.Bertucci[ac], A.Biland[ag], S.Bizzaglia[ac], S.Blasko[ac], G.Boella[z], M.Boschini[z], M.Bourquin[r], G.Bruni[j], M.Buenerd[s], J.D.Burger[l], W.J.Burger[ac], X.D.Cai[l], R.Cavalletti[j], C.Camps[b], P.Cannarsa[ag], M.Capell[l], D.Casadei[j], J.Casaus[y], G.Castellini[p], Y.H.Chang[m], H.F.Chen[t], H.S.Chen[i], Z.G.Chen[g], N.A.Chernoplekov[aa], A.Chiarini[j], T.H.Chiueh[m], Y.L.Chuang[ad], F.Cindolo[j], V.Commichau[b], A.Contin[j], A.Cotta–Ramusino[j], P.Crespo[w], M.Cristinziani[r], J.P.da Cunha[n], T.S.Dai[l], J.D.Deus[y], N.Dinu[ac,1], L.Djambazov[ag], I.D'Antone[j], Z.R.Dong[h], P.Emonet[r], J.Engelberg[u], F.J.Eppling[l], T.Eronen[af], G.Esposito[ac], P.Extermann[r], J.Favier[c], C.C.Feng[x], E.Fiandrini[ac], F.Finelli[j], P.H.Fisher[l], R.Flaminio[c], G.Fluegge[b], N.Fouque[c], Yu.Galaktionov[ab,l], M.Gervasi[z], P.Giusti[j], D.Grandi[z], W.Q.Gu[h], K.Hangarter[b], A.Hasan[ag], V.Hermel[c], H.Hofer[ag], M.A.Huang[ad], W.Hungerford[ag], M.Ionica[ac,1], R.Ionica[ac,1], M.Jongmanns[ag], K.Karlamaa[u], W.Karpinski[a], G.Kenney[ag], J.Kenny[ac], W.Kim[ae], A.Klimentov[l,ab], R.Kossakowski[c], V.Koutsenko[l,ab], G.Laborie[s], T.Laitinen[af], G.Lamanna[ac], G.Laurenti[j], A.Lebedev[l], S.C.Lee[ad], G.Levi[j], P.Levtchenko[ac,2], C.L.Liu[x], H.T.Liu[i], M.Lolli[j], I.Lopes[n], G.Lu[g], Y.S.Lu[i], K.Lübelsmeyer[a], D.Luckey[l], W.Lustermann[ag], C.Maña[y], A.Margotti[j], F.Massera[j], F.Mayet[s], R.R.McNeil[e], B.Meillon[s], M.Menichelli[ac], F.Mezzanotte[j], R.Mezzenga[ac], A.Mihul[k], G.Molinari[j], A.Mourao[v], A.Mujunen[u], F.Palmonari[j], G.Pancaldi[j], A.Papi[ac], I.H.Park[ae], M.Pauluzzi[ac], F.Pauss[ag], E.Perrin[r], A.Pesci[j], A.Pevsner[d], R.Pilastrini[j], M.Pimenta[w,v], V.Plyaskin[ab], V.Pojidaev[ab], H.Postema[l,3], V.Postolache[ac,1], E.Prati[j], N.Produit[r], P.G.Rancoita[z], D.Rapin[r], F.Raupach[a], S.Recupero[j], D.Ren[ag], Z.Ren[ad], M.Ribordy[r], J.P.Richeux[r], E.Riihonen[af], J.Ritakari[u], U.Roeser[ag], C.Roissin[s], R.Sagdeev[o], D.Santos[s], G.Sartorelli[j], A.Schultz von Dratzig[a], G.Schwering[a], E.S.Seo[o], V.Shoutko[l], E.Shoumilov[ab], R.Siedling[a], D.Son[ae], T.Song[h], M.Steuer[l], G.S.Sun[h], H.Suter[ag], X.W.Tang[i], Samuel C.C.Ting[l], S.M.Ting[l], M.Tornikoski[u], G.Torromeo[j], J.Torsti[af], J.Trümper[q], J.Ulbricht[ag], S.Urpo[u], I.Usoskin[z], E.Valtonen[af], J.Vandenhirtz[a], F.Velcea[ac,1], E.Velikhov[aa], B.Verlaat[ag,4], I.Vetlitsky[ab], F.Vezzu[s], J.P.Vialle[c], G.Viertel[ag], D.Vité[r], H.Von Gunten[ag], S.Waldmeier Wicki[ag], W.Wallraff[a], B.C.Wang[x], J.Z.Wang[g], Y.H.Wang[ad], K.Wiik[u], C.Williams[j], S.X.Wu[l,m], P.C.Xia[h], J.L.Yan[g], L.G.Yan[h], C.G.Yang[i], M.Yang[i], S.W.Ye[t,5], P.Yeh[ad], Z.Z.Xu[t], H.Y.Zhang[f], Z.P.Zhang[t], D.X.Zhao[h], G.Y.Zhu[i], W.Z.Zhu[g], H.L.Zhuang[i], A.Zichichi[j].

---

[a] I. Physikalisches Institut, RWTH, D-52056 Aachen, Germany[6]

[b] III. Physikalisches Institut, RWTH, D-52056 Aachen, Germany[6]

[c] Laboratoire d'Annecy-le-Vieux de Physique des Particules, LAPP, F-74941 Annecy-le-Vieux CEDEX, France

[e] Louisiana State University, Baton Rouge, LA 70803, USA

[d] Johns Hopkins University, Baltimore, MD 21218, USA

[f] Center of Space Science and Application, Chinese Academy of Sciences, 100080 Beijing, China

[g] Chinese Academy of Launching Vehicle Technology, CALT, 100076 Beijing, China

[h] Institute of Electrical Engineering, IEE, Chinese Academy of Sciences, 100080 Beijing, China

[i] Institute of High Energy Physics, IHEP, Chinese Academy of Sciences, 100039 Beijing, China[7]

[j] University of Bologna and INFN-Sezione di Bologna, I-40126 Bologna, Italy

[k] Institute of Microtechnology, Politechnica University of Bucharest and University of Bucharest, R-76900 Bucharest, Romania

[l] Massachusetts Institute of Technology, Cambridge, MA 02139, USA

[m] National Central University, Chung-Li, Taiwan 32054

[n] Laboratorio de Instrumentacao e Fisica Experimental de Particulas, LIP, P-3000 Coimbra, Portugal

[o] University of Maryland, College Park, MD 20742, USA

[p] INFN Sezione di Firenze, I-50125 Florence, Italy

[q] Max–Plank Institut fur Extraterrestrische Physik, D-85740 Garching, Germany
[r] University of Geneva, CH-1211 Geneva 4, Switzerland
[s] Institut des Sciences Nucleaires, F-38026 Grenoble, France
[t] Chinese University of Science and Technology, USTC, Hefei, Anhui 230 029, China[7]
[u] Helsinki University of Technology, FIN-02540 Kylmala, Finland
[v] Instituto Superior Técnico, IST, P-1096 Lisboa, Portugal
[w] Laboratorio de Instrumentacao e Fisica Experimental de Particulas, LIP, P-1000 Lisboa, Portugal
[x] Chung–Shan Institute of Science and Technology, Lung-Tan, Tao Yuan 325, Taiwan 11529
[y] Centro de Investigaciones Energéticas, Medioambientales y Tecnologícas, CIEMAT, E-28040 Madrid, Spain[8]
[z] INFN-Sezione di Milano, I-20133 Milan, Italy
[aa] Kurchatov Institute, Moscow, 123182 Russia
[ab] Institute of Theoretical and Experimental Physics, ITEP, Moscow, 117259 Russia
[ac] INFN-Sezione di Perugia and Universitá Degli Studi di Perugia, I-06100 Perugia, Italy[9]
[ad] Academia Sinica, Taipei, Taiwan
[ae] Kyungpook National University, 702-701 Taegu, Korea
[af] University of Turku, FIN-20014 Turku, Finland
[ag] Eidgenössische Technische Hochschule, ETH Zürich, CH-8093 Zürich, Switzerland
[1] Permanent address: HEPPG, Univ. of Bucharest, Romania.
[2] Permanent address: Nuclear Physics Institute, St. Petersburg, Russia.
[3] Now at European Laboratory for Particle Physics, CERN, CH-1211 Geneva 23, Switzerland.
[4] Now at National Institute for High Energy Physics, NIKHEF, NL-1009 DB Amsterdam, The Netherlands.
[5] Supported by ETH Zürich.
[6] Supported by the Deutsches Zentrum für Luft– und Raumfahrt, DLR.
[7] Supported by the National Natural Science Foundation of China.
[8] Supported also by the Comisión Interministerial de Ciencia y Tecnología.
[9] Also supported by the Italian Space Agency.

Downward Proton Flux $(m^2\,sec\,sr\,MeV)^{-1}$						
E_{kin} (GeV)		Geomagnetic Latitude Range				
		$\Theta_M < 0.2$	$0.2 \le \Theta_M < 0.3$	$0.3 \le \Theta_M < 0.4$	$0.4 \le \Theta_M < 0.5$	$0.5 \le \Theta_M < 0.6$
0.07 –	0.10	$(16.7\pm4.4)\times10^{-2}$	$(14.2\pm4.0)\times10^{-2}$	$(11.2\pm3.1)\times10^{-2}$	$(13.6\pm3.8)\times10^{-2}$	$(13.4\pm3.6)\times10^{-2}$
0.10 –	0.15	$(12.1\pm1.4)\times10^{-2}$	$(\ 8.2\pm1.0)\times10^{-2}$	$(\ 7.6\pm1.0)\times10^{-2}$	$(\ 7.6\pm1.0)\times10^{-2}$	$(\ 7.7\pm1.0)\times10^{-2}$
0.15 –	0.22	$(97.9\pm4.6)\times10^{-3}$	$(51.2\pm3.2)\times10^{-3}$	$(41.9\pm2.6)\times10^{-3}$	$(44.6\pm3.0)\times10^{-3}$	$(48.4\pm3.3)\times10^{-3}$
0.22 –	0.31	$(86.2\pm2.8)\times10^{-3}$	$(45.6\pm1.8)\times10^{-3}$	$(37.9\pm1.7)\times10^{-3}$	$(34.4\pm1.5)\times10^{-3}$	$(32.7\pm1.6)\times10^{-3}$
0.31 –	0.44	$(70.1\pm3.2)\times10^{-3}$	$(34.6\pm1.5)\times10^{-3}$	$(24.4\pm1.1)\times10^{-3}$	$(21.1\pm1.2)\times10^{-3}$	$(20.2\pm1.2)\times10^{-3}$
0.44 –	0.62	$(50.4\pm2.7)\times10^{-3}$	$(21.2\pm1.2)\times10^{-3}$	$(155.\pm9.3)\times10^{-4}$	$(121.\pm9.3)\times10^{-4}$	$(113.\pm9.0)\times10^{-4}$
0.62 –	0.85	$(32.8\pm1.9)\times10^{-3}$	$(116.\pm6.8)\times10^{-4}$	$(84.9\pm6.5)\times10^{-4}$	$(61.5\pm5.6)\times10^{-4}$	$(50.0\pm6.4)\times10^{-4}$
0.85 –	1.15	$(20.6\pm1.2)\times10^{-3}$	$(57.2\pm4.7)\times10^{-4}$	$(40.0\pm3.8)\times10^{-4}$	$(26.9\pm3.4)\times10^{-4}$	$(24.2\pm4.2)\times10^{-4}$
1.15 –	1.54	$(116.\pm6.9)\times10^{-4}$	$(28.6\pm3.3)\times10^{-4}$	$(17.7\pm2.5)\times10^{-4}$	$(12.7\pm2.9)\times10^{-4}$	$(\ 8.5\pm1.4)\times10^{-4}$
1.54 –	2.02	$(66.9\pm4.2)\times10^{-4}$	$(12.2\pm2.1)\times10^{-4}$	$(\ 8.5\pm2.6)\times10^{-4}$	$(\ 6.9\pm1.4)\times10^{-4}$	$(\ 5.7\pm1.0)\times10^{-4}$
2.02 –	2.62	$(28.6\pm1.9)\times10^{-4}$	$(\ 8.2\pm1.8)\times10^{-4}$	$(\ 5.0\pm1.3)\times10^{-4}$	$(37.3\pm3.3)\times10^{-5}$	$(34.2\pm1.5)\times10^{-5}$
2.62 –	3.38	$(110.\pm9.6)\times10^{-5}$	$(\ 3.6\pm1.1)\times10^{-4}$	$(30.0\pm8.6)\times10^{-5}$	$(204.\pm7.4)\times10^{-6}$	$(29.0\pm1.4)\times10^{-5}$
3.38 –	4.31	$(44.3\pm7.9)\times10^{-5}$	$(20.3\pm6.0)\times10^{-5}$	$(23.2\pm3.6)\times10^{-5}$	$(25.0\pm1.3)\times10^{-5}$	$(10.7\pm1.1)\times10^{-4}$
4.31 –	5.45	$(15.7\pm3.1)\times10^{-5}$	$(13.4\pm4.8)\times10^{-5}$	$(17.6\pm3.2)\times10^{-5}$	$(58.5\pm5.9)\times10^{-5}$	$(62.9\pm6.4)\times10^{-4}$
5.45 –	6.86	$(\ 6.1\pm2.2)\times10^{-5}$	$(105.\pm8.7)\times10^{-6}$	$(31.9\pm2.3)\times10^{-5}$	$(32.1\pm3.0)\times10^{-4}$	$(18.4\pm1.4)\times10^{-3}$
6.86 –	8.60	$(23.7\pm2.1)\times10^{-5}$	$(53.8\pm2.7)\times10^{-5}$	$(19.5\pm1.5)\times10^{-4}$	$(96.2\pm6.4)\times10^{-4}$	$(23.3\pm1.2)\times10^{-3}$
8.60 –	10.73	$(138.\pm6.8)\times10^{-5}$	$(28.6\pm1.7)\times10^{-4}$	$(58.5\pm3.3)\times10^{-4}$	$(128.\pm5.4)\times10^{-4}$	$(193.\pm5.1)\times10^{-4}$
10.73 –	13.34	$(49.5\pm1.8)\times10^{-4}$	$(60.9\pm2.4)\times10^{-4}$	$(85.7\pm3.1)\times10^{-4}$	$(115.\pm2.8)\times10^{-4}$	$(128.\pm3.7)\times10^{-4}$
13.34 –	16.55	$(65.7\pm2.1)\times10^{-4}$	$(63.4\pm1.8)\times10^{-4}$	$(72.1\pm2.1)\times10^{-4}$	$(75.6\pm2.5)\times10^{-4}$	$(75.6\pm2.7)\times10^{-4}$
16.55 –	20.48	$(45.7\pm1.7)\times10^{-4}$	$(45.5\pm1.7)\times10^{-4}$	$(44.4\pm1.5)\times10^{-4}$	$(45.2\pm1.8)\times10^{-4}$	$(43.3\pm1.2)\times10^{-4}$
20.48 –	25.29	$(27.7\pm1.0)\times10^{-4}$	$(25.5\pm1.0)\times10^{-4}$	$(255.\pm9.8)\times10^{-5}$	$(248.\pm9.6)\times10^{-5}$	$(24.0\pm1.0)\times10^{-4}$
25.29 –	31.20	$(155.\pm5.9)\times10^{-5}$	$(147.\pm7.1)\times10^{-5}$	$(144.\pm6.8)\times10^{-5}$	$(142.\pm6.7)\times10^{-5}$	$(138.\pm5.6)\times10^{-5}$
31.20 –	38.43	$(90.5\pm4.1)\times10^{-5}$	$(79.2\pm4.7)\times10^{-5}$	$(80.5\pm4.5)\times10^{-5}$	$(80.0\pm4.3)\times10^{-5}$	$(77.1\pm4.3)\times10^{-5}$
38.43 –	47.30	$(51.4\pm2.2)\times10^{-5}$	$(48.9\pm3.0)\times10^{-5}$	$(48.2\pm2.5)\times10^{-5}$	$(48.2\pm3.0)\times10^{-5}$	$(47.1\pm2.7)\times10^{-5}$
47.30 –	58.16	$(30.0\pm1.7)\times10^{-5}$	$(28.6\pm2.0)\times10^{-5}$	$(28.7\pm1.8)\times10^{-5}$	$(28.4\pm1.8)\times10^{-5}$	$(27.7\pm1.8)\times10^{-5}$
58.16 –	71.48	$(164.\pm8.8)\times10^{-6}$	$(15.4\pm1.2)\times10^{-5}$	$(15.6\pm1.2)\times10^{-5}$	$(154.\pm8.8)\times10^{-6}$	$(149.\pm9.9)\times10^{-6}$
71.48 –	87.79	$(86.1\pm3.9)\times10^{-6}$	$(79.6\pm4.7)\times10^{-6}$	$(81.5\pm6.4)\times10^{-6}$	$(80.2\pm5.9)\times10^{-6}$	$(76.7\pm5.1)\times10^{-6}$
87.79 –	107.78	$(49.4\pm2.9)\times10^{-6}$	$(45.0\pm4.6)\times10^{-6}$	$(46.6\pm4.8)\times10^{-6}$	$(45.8\pm2.8)\times10^{-6}$	$(43.4\pm2.6)\times10^{-6}$
107.78 –	132.27	$(28.6\pm3.1)\times10^{-6}$	$(25.7\pm6.1)\times10^{-6}$	$(26.9\pm7.3)\times10^{-6}$	$(26.4\pm6.2)\times10^{-6}$	$(24.8\pm4.6)\times10^{-6}$
132.27 –	162.29	$(16.2\pm1.8)\times10^{-6}$	$(14.3\pm7.0)\times10^{-6}$	$(15.2\pm5.2)\times10^{-6}$	$(14.9\pm7.9)\times10^{-6}$	$(13.8\pm6.3)\times10^{-6}$
162.29 –	199.06	$(97.2\pm5.1)\times10^{-7}$	$(84.8\pm6.7)\times10^{-7}$	$(\ 9.1\pm2.3)\times10^{-6}$	$(\ 8.9\pm1.8)\times10^{-6}$	$(82.1\pm6.2)\times10^{-7}$

Table 2: Differential downward proton flux spectra for lower latitudes.

Downward Proton Flux $(m^2\,sec\,sr\,MeV)^{-1}$						
E_{kin} (GeV)		Geomagnetic Latitude Range				
		$0.6 \le \Theta_M < 0.7$	$0.7 \le \Theta_M < 0.8$	$0.8 \le \Theta_M < 0.9$	$0.9 \le \Theta_M < 1.0$	$1.0 \le \Theta_M$
0.07 –	0.10	$(12.2\pm3.5)\times10^{-2}$	$(18.5\pm5.9)\times10^{-2}$	$(25.1\pm8.9)\times10^{-2}$	$(\ 4.3\pm1.3)\times10^{-1}$	$(\ 9.2\pm2.6)\times10^{-1}$
0.10 –	0.15	$(\ 9.7\pm1.3)\times10^{-2}$	$(11.8\pm1.6)\times10^{-2}$	$(19.1\pm2.6)\times10^{-2}$	$(41.8\pm5.6)\times10^{-2}$	$(\ 9.8\pm1.2)\times10^{-1}$
0.15 –	0.22	$(66.0\pm3.7)\times10^{-3}$	$(97.3\pm5.9)\times10^{-3}$	$(144.\pm8.9)\times10^{-3}$	$(33.6\pm3.3)\times10^{-2}$	$(109.\pm6.7)\times10^{-2}$
0.22 –	0.31	$(44.4\pm1.6)\times10^{-3}$	$(44.2\pm2.0)\times10^{-3}$	$(92.4\pm6.9)\times10^{-3}$	$(22.6\pm3.9)\times10^{-2}$	$(126.\pm5.3)\times10^{-2}$
0.31 –	0.44	$(24.1\pm1.7)\times10^{-3}$	$(23.8\pm1.3)\times10^{-3}$	$(58.3\pm4.8)\times10^{-3}$	$(29.3\pm7.1)\times10^{-2}$	$(139.\pm4.1)\times10^{-2}$
0.44 –	0.62	$(108.\pm8.8)\times10^{-4}$	$(14.4\pm1.0)\times10^{-3}$	$(36.6\pm3.5)\times10^{-3}$	$(\ 4.7\pm1.1)\times10^{-1}$	$(132.\pm4.8)\times10^{-2}$
0.62 –	0.85	$(47.8\pm6.7)\times10^{-4}$	$(77.2\pm6.9)\times10^{-4}$	$(22.0\pm2.5)\times10^{-3}$	$(\ 7.5\pm1.3)\times10^{-1}$	$(114.\pm4.2)\times10^{-2}$
0.85 –	1.15	$(23.1\pm4.9)\times10^{-4}$	$(60.9\pm6.5)\times10^{-4}$	$(34.9\pm5.8)\times10^{-3}$	$(85.3\pm7.5)\times10^{-2}$	$(92.8\pm3.2)\times10^{-2}$
1.15 –	1.54	$(13.1\pm2.2)\times10^{-4}$	$(23.7\pm2.9)\times10^{-4}$	$(15.4\pm2.4)\times10^{-2}$	$(71.7\pm4.5)\times10^{-2}$	$(72.4\pm2.4)\times10^{-2}$
1.54 –	2.02	$(\ 7.7\pm1.2)\times10^{-4}$	$(44.8\pm6.7)\times10^{-4}$	$(28.1\pm3.3)\times10^{-2}$	$(52.4\pm4.5)\times10^{-2}$	$(51.1\pm1.4)\times10^{-2}$
2.02 –	2.62	$(77.7\pm8.3)\times10^{-5}$	$(43.1\pm5.8)\times10^{-3}$	$(30.9\pm1.8)\times10^{-2}$	$(36.2\pm2.9)\times10^{-2}$	$(37.0\pm1.1)\times10^{-2}$
2.62 –	3.38	$(49.1\pm5.9)\times10^{-4}$	$(11.4\pm1.1)\times10^{-2}$	$(22.6\pm1.4)\times10^{-2}$	$(24.8\pm2.1)\times10^{-2}$	$(241.\pm6.4)\times10^{-3}$
3.38 –	4.31	$(27.9\pm2.9)\times10^{-3}$	$(124.\pm4.6)\times10^{-3}$	$(15.4\pm1.1)\times10^{-2}$	$(16.2\pm1.1)\times10^{-2}$	$(163.\pm3.1)\times10^{-3}$
4.31 –	5.45	$(56.4\pm4.0)\times10^{-3}$	$(88.4\pm4.3)\times10^{-3}$	$(95.3\pm5.9)\times10^{-3}$	$(103.\pm7.7)\times10^{-3}$	$(102.\pm2.9)\times10^{-3}$
5.45 –	6.86	$(52.6\pm1.7)\times10^{-3}$	$(55.6\pm3.2)\times10^{-3}$	$(59.3\pm3.5)\times10^{-3}$	$(63.8\pm5.0)\times10^{-3}$	$(61.4\pm1.3)\times10^{-3}$
6.86 –	8.60	$(35.6\pm1.2)\times10^{-3}$	$(34.0\pm1.8)\times10^{-3}$	$(36.3\pm2.6)\times10^{-3}$	$(39.0\pm2.8)\times10^{-3}$	$(390.\pm8.2)\times10^{-4}$
8.60 –	10.73	$(212.\pm9.0)\times10^{-4}$	$(20.2\pm1.1)\times10^{-3}$	$(21.8\pm1.6)\times10^{-3}$	$(22.5\pm1.6)\times10^{-3}$	$(223.\pm6.5)\times10^{-4}$
10.73 –	13.34	$(129.\pm5.3)\times10^{-4}$	$(121.\pm6.4)\times10^{-4}$	$(128.\pm8.0)\times10^{-4}$	$(14.1\pm1.3)\times10^{-3}$	$(136.\pm4.5)\times10^{-4}$
13.34 –	16.55	$(75.8\pm3.3)\times10^{-4}$	$(69.0\pm3.8)\times10^{-4}$	$(75.2\pm4.3)\times10^{-4}$	$(78.0\pm5.7)\times10^{-4}$	$(76.2\pm2.7)\times10^{-4}$
16.55 –	20.48	$(41.7\pm1.5)\times10^{-4}$	$(40.5\pm2.1)\times10^{-4}$	$(40.2\pm3.0)\times10^{-4}$	$(39.3\pm3.3)\times10^{-4}$	$(39.6\pm1.3)\times10^{-4}$
20.48 –	25.29	$(24.9\pm1.1)\times10^{-4}$	$(22.7\pm1.3)\times10^{-4}$	$(237.\pm8.0)\times10^{-5}$	$(23.8\pm2.0)\times10^{-4}$	$(22.0\pm1.3)\times10^{-4}$
25.29 –	31.20	$(134.\pm5.6)\times10^{-5}$	$(132.\pm8.7)\times10^{-5}$	$(127.\pm6.4)\times10^{-5}$	$(12.3\pm1.4)\times10^{-4}$	$(118.\pm7.9)\times10^{-5}$
31.20 –	38.43	$(75.1\pm4.0)\times10^{-5}$	$(69.2\pm4.5)\times10^{-5}$	$(61.5\pm5.7)\times10^{-5}$	$(78.0\pm8.8)\times10^{-5}$	$(76.7\pm6.5)\times10^{-5}$
38.43 –	47.30	$(46.0\pm2.7)\times10^{-5}$	$(44.7\pm2.8)\times10^{-5}$	$(44.0\pm3.5)\times10^{-5}$	$(44.1\pm4.6)\times10^{-5}$	$(47.7\pm3.7)\times10^{-5}$
47.30 –	58.16	$(27.0\pm1.8)\times10^{-5}$	$(26.3\pm1.9)\times10^{-5}$	$(25.7\pm2.8)\times10^{-5}$	$(27.0\pm2.6)\times10^{-5}$	$(28.5\pm2.6)\times10^{-5}$
58.16 –	71.48	$(14.6\pm1.2)\times10^{-5}$	$(142.\pm9.9)\times10^{-6}$	$(13.9\pm1.3)\times10^{-5}$	$(14.3\pm1.5)\times10^{-5}$	$(154.\pm9.8)\times10^{-6}$
71.48 –	87.79	$(76.0\pm4.6)\times10^{-6}$	$(72.9\pm4.5)\times10^{-6}$	$(71.7\pm6.4)\times10^{-6}$	$(72.5\pm6.5)\times10^{-6}$	$(79.3\pm8.7)\times10^{-6}$
87.79 –	107.78	$(43.5\pm5.8)\times10^{-6}$	$(41.5\pm3.0)\times10^{-6}$	$(41.1\pm4.1)\times10^{-6}$	$(40.3\pm6.3)\times10^{-6}$	$(44.8\pm7.9)\times10^{-6}$
107.78 –	132.27	$(25.2\pm4.5)\times10^{-6}$	$(23.9\pm4.4)\times10^{-6}$	$(23.9\pm4.4)\times10^{-6}$	$(\ 2.3\pm1.2)\times10^{-5}$	$(\ 2.6\pm1.2)\times10^{-5}$
132.27 –	162.29	$(14.3\pm3.9)\times10^{-6}$	$(13.4\pm4.7)\times10^{-6}$	$(13.6\pm6.5)\times10^{-6}$	$(12.3\pm8.9)\times10^{-6}$	$(\ 1.4\pm1.4)\times10^{-5}$
162.29 –	199.06	$(\ 8.6\pm1.5)\times10^{-6}$	$(80.6\pm4.3)\times10^{-7}$	$(\ 8.2\pm1.3)\times10^{-6}$	$(\ 7.2\pm3.7)\times10^{-6}$	$(\ 8.5\pm2.4)\times10^{-6}$

Table 3: Differential downward proton flux spectra for higher latitudes.

Upward Proton Flux $(m^2\,sec\,sr\,MeV)^{-1}$					
E_{kin}	Geomagnetic Latitude Range				
(GeV)	$\Theta_M < 0.2$	$0.2 \le \Theta_M < 0.3$	$0.3 \le \Theta_M < 0.4$	$0.4 \le \Theta_M < 0.5$	$0.5 \le \Theta_M < 0.6$
0.07 – 0.10	$(16.4\pm4.4)\times10^{-2}$	$(13.1\pm3.9)\times10^{-2}$	$(12.6\pm3.5)\times10^{-2}$	$(14.7\pm4.1)\times10^{-2}$	$(15.8\pm4.7)\times10^{-2}$
0.10 – 0.15	$(10.9\pm1.4)\times10^{-2}$	$(7.5\pm1.0)\times10^{-2}$	$(66.0\pm9.2)\times10^{-3}$	$(7.7\pm1.1)\times10^{-2}$	$(8.7\pm1.2)\times10^{-2}$
0.15 – 0.22	$(85.3\pm4.9)\times10^{-3}$	$(48.1\pm3.5)\times10^{-3}$	$(42.7\pm2.8)\times10^{-3}$	$(42.2\pm2.8)\times10^{-3}$	$(46.3\pm2.8)\times10^{-3}$
0.22 – 0.31	$(84.8\pm3.8)\times10^{-3}$	$(44.5\pm2.1)\times10^{-3}$	$(39.3\pm1.9)\times10^{-3}$	$(35.5\pm1.8)\times10^{-3}$	$(34.6\pm1.5)\times10^{-3}$
0.31 – 0.44	$(66.8\pm3.4)\times10^{-3}$	$(33.6\pm1.7)\times10^{-3}$	$(25.4\pm1.1)\times10^{-3}$	$(21.4\pm1.1)\times10^{-3}$	$(21.0\pm1.1)\times10^{-3}$
0.44 – 0.62	$(48.4\pm2.7)\times10^{-3}$	$(20.3\pm1.2)\times10^{-3}$	$(136.\pm8.3)\times10^{-4}$	$(124.\pm9.2)\times10^{-4}$	$(97.6\pm8.1)\times10^{-4}$
0.62 – 0.85	$(32.7\pm2.0)\times10^{-3}$	$(120.\pm8.6)\times10^{-4}$	$(76.4\pm5.6)\times10^{-4}$	$(61.9\pm6.1)\times10^{-4}$	$(34.8\pm4.3)\times10^{-4}$
0.85 – 1.15	$(20.2\pm1.1)\times10^{-3}$	$(53.9\pm4.6)\times10^{-4}$	$(42.0\pm4.5)\times10^{-4}$	$(31.9\pm4.6)\times10^{-4}$	$(17.9\pm3.3)\times10^{-4}$
1.15 – 1.54	$(124.\pm7.1)\times10^{-4}$	$(34.8\pm4.4)\times10^{-4}$	$(14.7\pm1.8)\times10^{-4}$	$(14.0\pm2.3)\times10^{-4}$	$(8.6\pm2.1)\times10^{-4}$
1.54 – 2.02	$(62.0\pm4.2)\times10^{-4}$	$(16.4\pm2.3)\times10^{-4}$	$(12.5\pm2.3)\times10^{-4}$	$(8.8\pm1.8)\times10^{-4}$	$(5.2\pm1.2)\times10^{-4}$
2.02 – 2.62	$(25.9\pm1.8)\times10^{-4}$	$(7.9\pm1.3)\times10^{-4}$	$(5.6\pm1.1)\times10^{-4}$	$(4.6\pm1.2)\times10^{-4}$	$(3.4\pm1.1)\times10^{-4}$
2.62 – 3.38	$(10.7\pm1.5)\times10^{-4}$	$(4.2\pm1.2)\times10^{-4}$	$(29.9\pm8.7)\times10^{-5}$	$(38.3\pm10.)\times10^{-5}$	$(25.9\pm9.6)\times10^{-5}$
3.38 – 4.31	$(29.7\pm5.7)\times10^{-5}$	$(15.6\pm8.3)\times10^{-5}$	$(11.9\pm4.9)\times10^{-5}$	$(13.4\pm5.7)\times10^{-5}$	$(9.4\pm3.7)\times10^{-5}$
4.31 – 5.45	$(11.2\pm4.6)\times10^{-5}$	$(6.4\pm4.2)\times10^{-5}$	$(7.2\pm3.8)\times10^{-5}$	$(6.4\pm3.3)\times10^{-5}$	
5.45 – 6.86	$(3.7\pm2.4)\times10^{-5}$				

E_{kin}	Geomagnetic Latitude Range				
(GeV)	$0.6 \le \Theta_M < 0.7$	$0.7 \le \Theta_M < 0.8$	$0.8 \le \Theta_M < 0.9$	$0.9 \le \Theta_M < 1.0$	
0.07 – 0.10	$(23.1\pm6.8)\times10^{-2}$	$(32.9\pm9.5)\times10^{-2}$	$(3.8\pm1.1)\times10^{-1}$	$(5.1\pm1.5)\times10^{-1}$	
0.10 – 0.15	$(10.5\pm1.5)\times10^{-2}$	$(15.4\pm2.3)\times10^{-2}$	$(18.0\pm2.4)\times10^{-2}$	$(25.5\pm4.1)\times10^{-2}$	
0.15 – 0.22	$(58.1\pm3.8)\times10^{-3}$	$(72.5\pm5.4)\times10^{-3}$	$(91.9\pm6.2)\times10^{-3}$	$(99.8\pm8.4)\times10^{-3}$	
0.22 – 0.31	$(43.0\pm2.1)\times10^{-3}$	$(44.8\pm3.4)\times10^{-3}$	$(57.4\pm3.3)\times10^{-3}$	$(54.0\pm4.9)\times10^{-3}$	
0.31 – 0.44	$(20.7\pm1.1)\times10^{-3}$	$(21.7\pm1.9)\times10^{-3}$	$(25.7\pm2.6)\times10^{-3}$	$(22.5\pm2.9)\times10^{-3}$	
0.44 – 0.62	$(83.4\pm8.0)\times10^{-4}$	$(78.6\pm9.3)\times10^{-4}$	$(8.8\pm1.2)\times10^{-3}$	$(8.8\pm1.7)\times10^{-3}$	
0.62 – 0.85	$(27.3\pm4.0)\times10^{-4}$	$(18.4\pm3.2)\times10^{-4}$	$(17.9\pm4.8)\times10^{-4}$	$(23.4\pm8.0)\times10^{-4}$	
0.85 – 1.15	$(7.2\pm2.3)\times10^{-4}$	$(4.9\pm1.9)\times10^{-4}$	$(7.4\pm4.2)\times10^{-4}$	$(12.6\pm5.1)\times10^{-4}$	
1.15 – 1.54	$(4.0\pm1.3)\times10^{-4}$	$(3.2\pm2.3)\times10^{-4}$	$(2.5\pm1.5)\times10^{-4}$	$(9.1\pm4.0)\times10^{-4}$	
1.54 – 2.02	$(3.0\pm1.4)\times10^{-4}$	$(11.6\pm7.2)\times10^{-5}$	$(1.3\pm1.2)\times10^{-4}$	$(16.8\pm9.3)\times10^{-5}$	
2.02 – 2.62	$(1.7\pm1.2)\times10^{-4}$	$(7.7\pm7.4)\times10^{-5}$			
2.62 – 3.38	$(6.3\pm4.1)\times10^{-5}$	$(4.8\pm3.8)\times10^{-5}$			
3.38 – 4.31	$(2.0\pm1.1)\times10^{-5}$				

Table 4: Differential upward proton flux spectra.

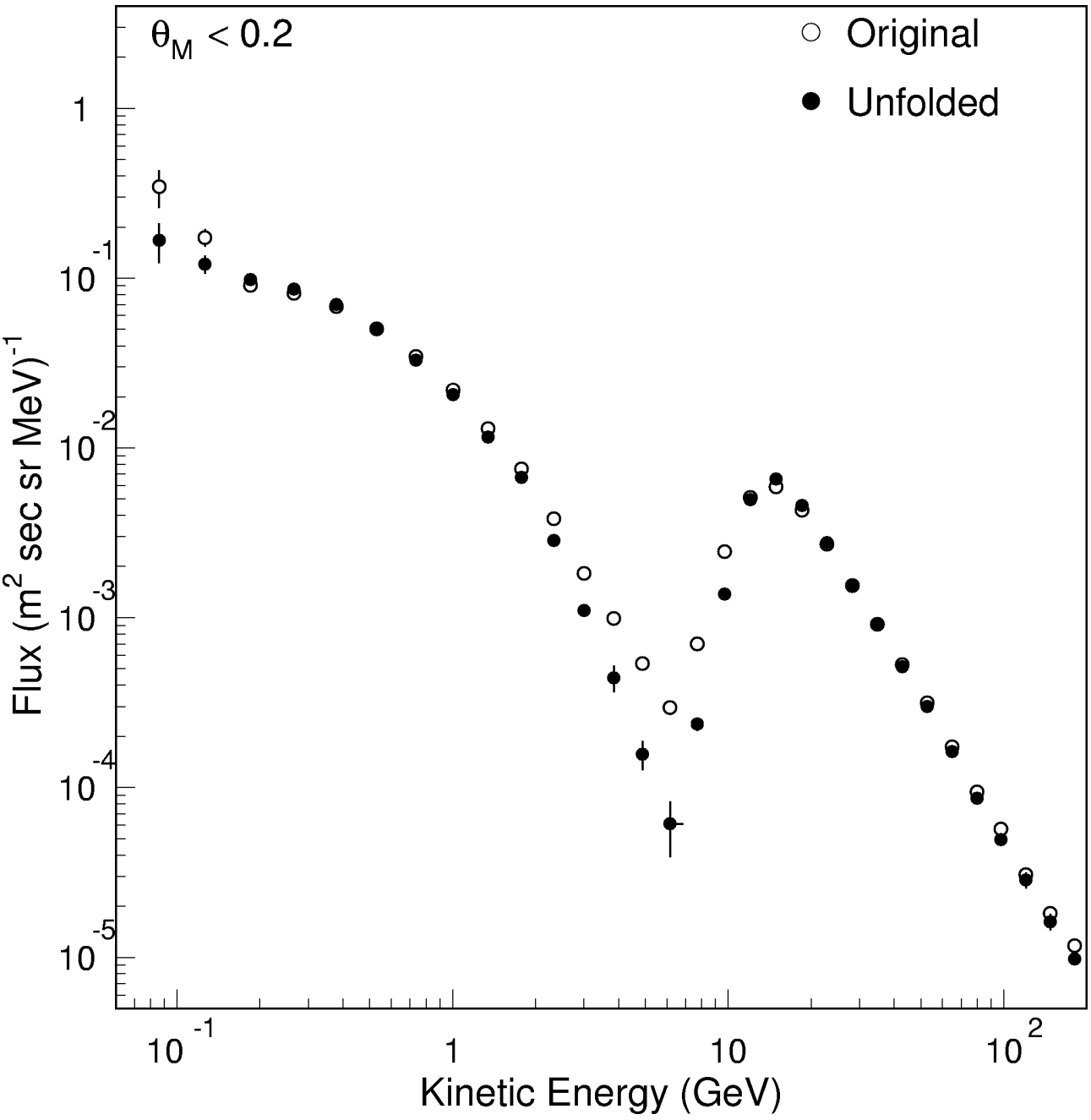

Figure 1: The proton differential flux in the equatorial region. Open circles show the measured distribution, filled circles are the data after unfolding.

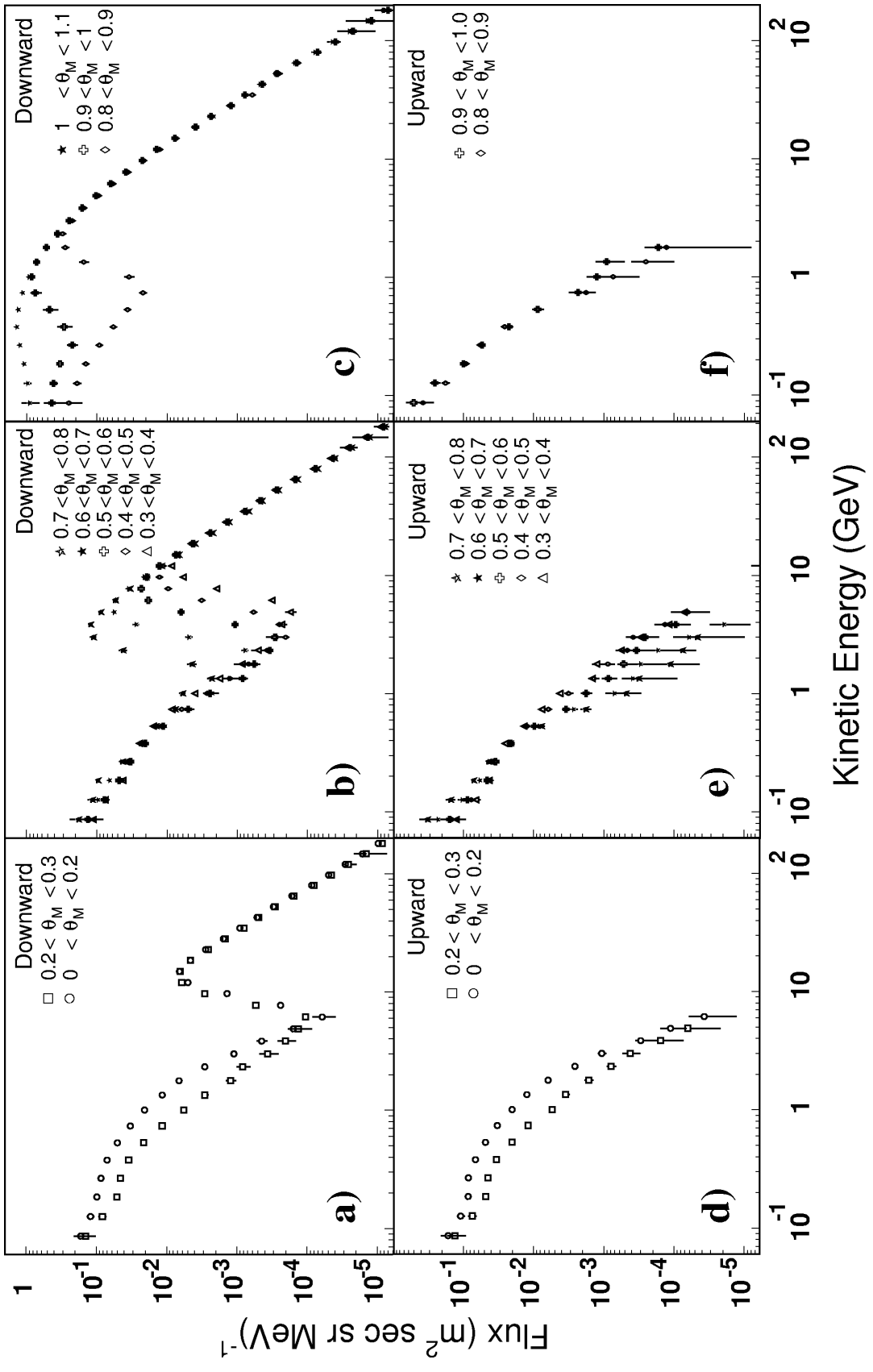

Figure 2: Flux spectra for a,b,c) downward and d,e,f) upward going protons seperated according to the geomagnetic latitude, Θ_M, at which they were detected.

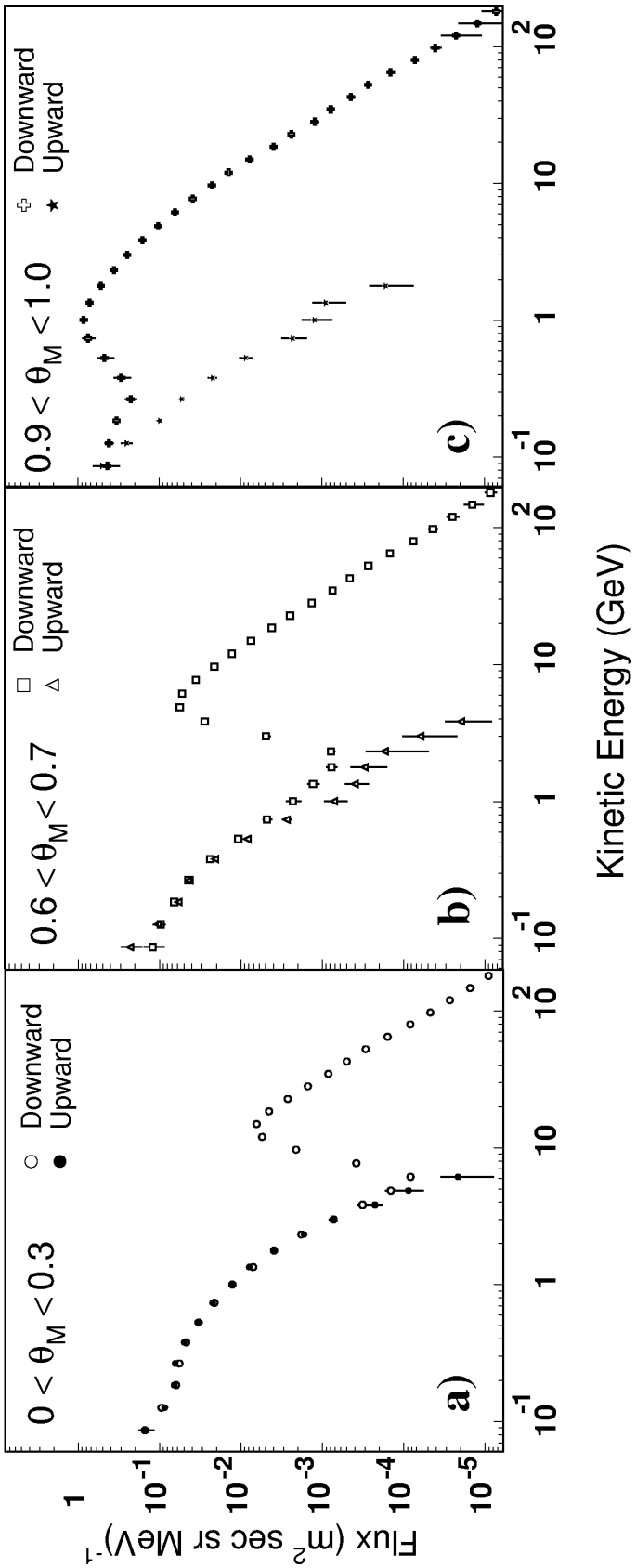

Figure 3: Comparison of upward and downward second spectrum proton at different geomagnetic latitudes. As seen, below cutoff, the upward and downward fluxes agree in the range $0 \leq \Theta_M < 0.8$ (see also Figs. 2b, e).

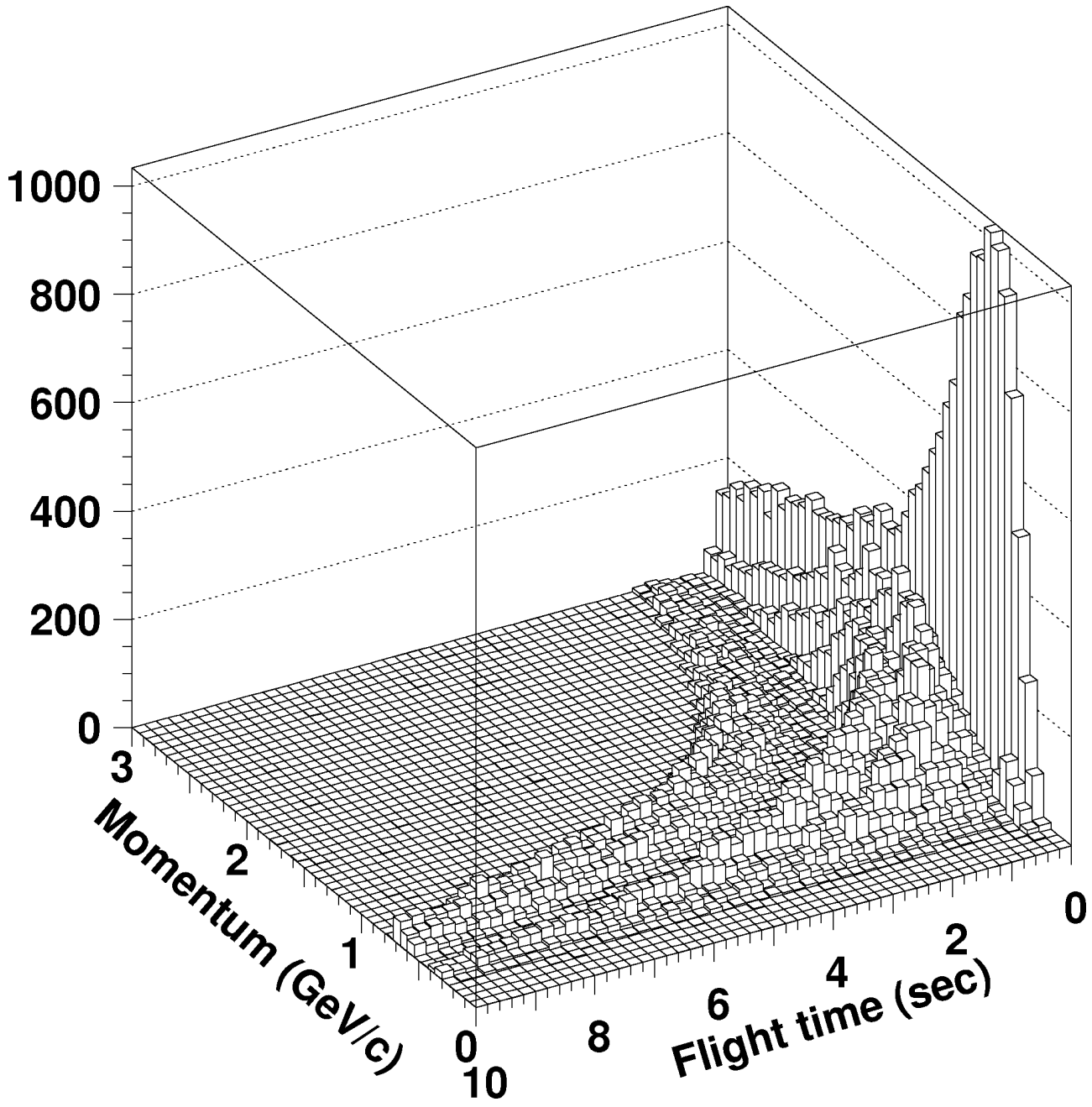

Figure 4: The interval between production and detection, or flight time, versus momentum from the back tracing of protons detected in the region $\Theta_M < 0.3$.

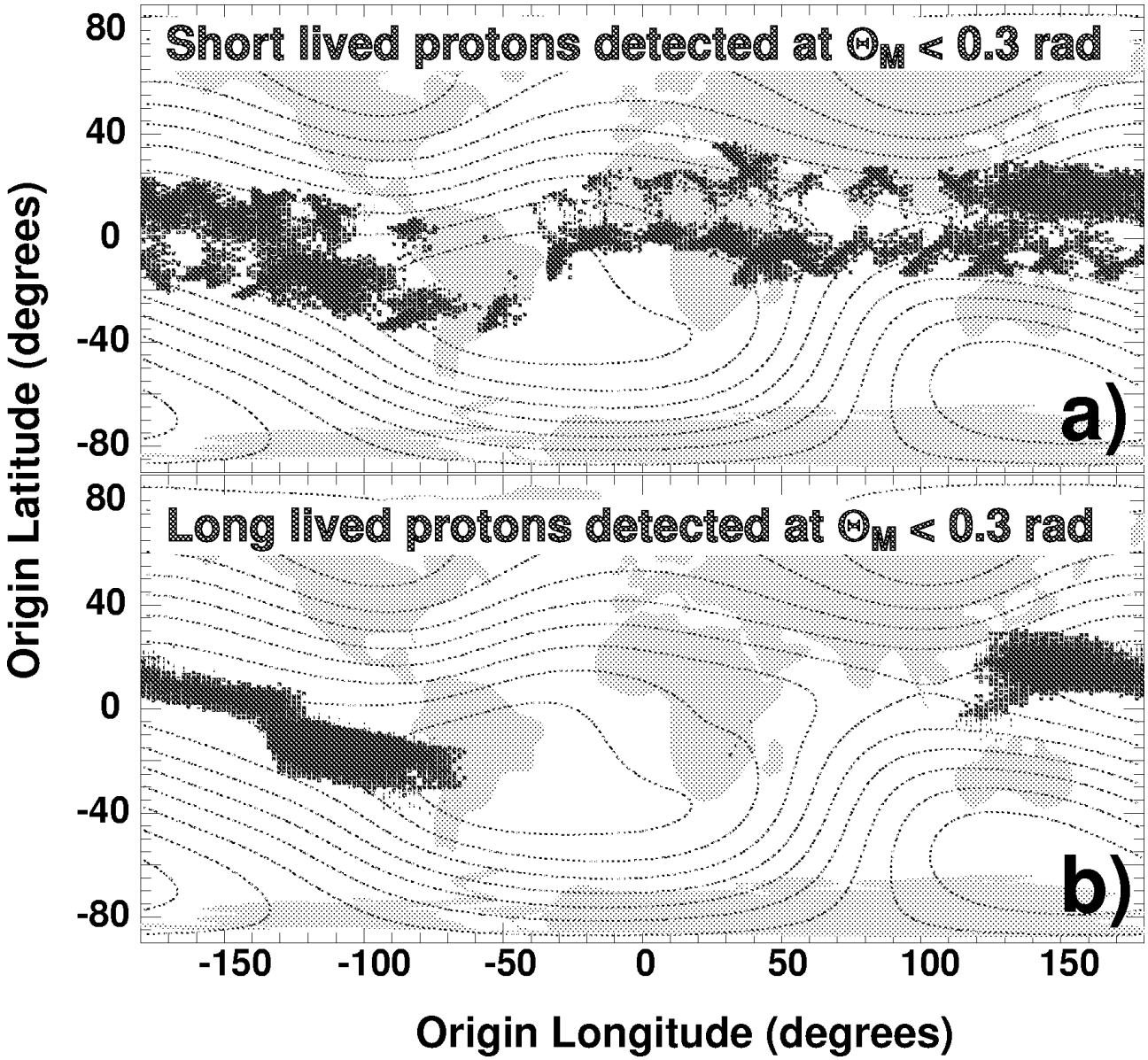

Figure 5: The geographical origin of a) short–lived and b) long–lived protons with $p < 3$ GeV/c. The dashed lines indicate the geomagnetic field countours at 380 km.

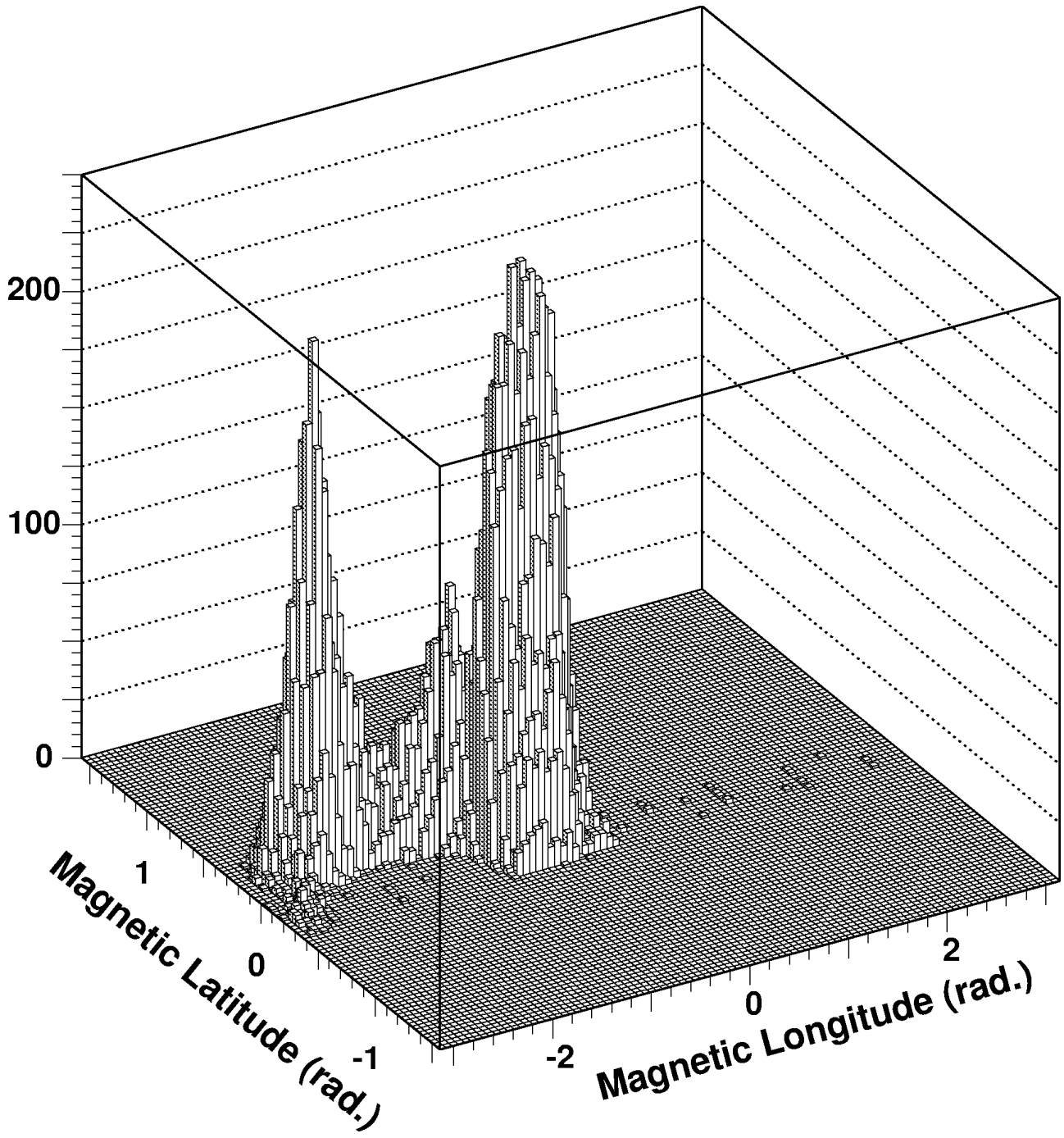

Figure 6: The point of origin of long–lived protons ($\Theta_M < 0.3, p < 3$ GeV/c) in geomagnetic coordinates.

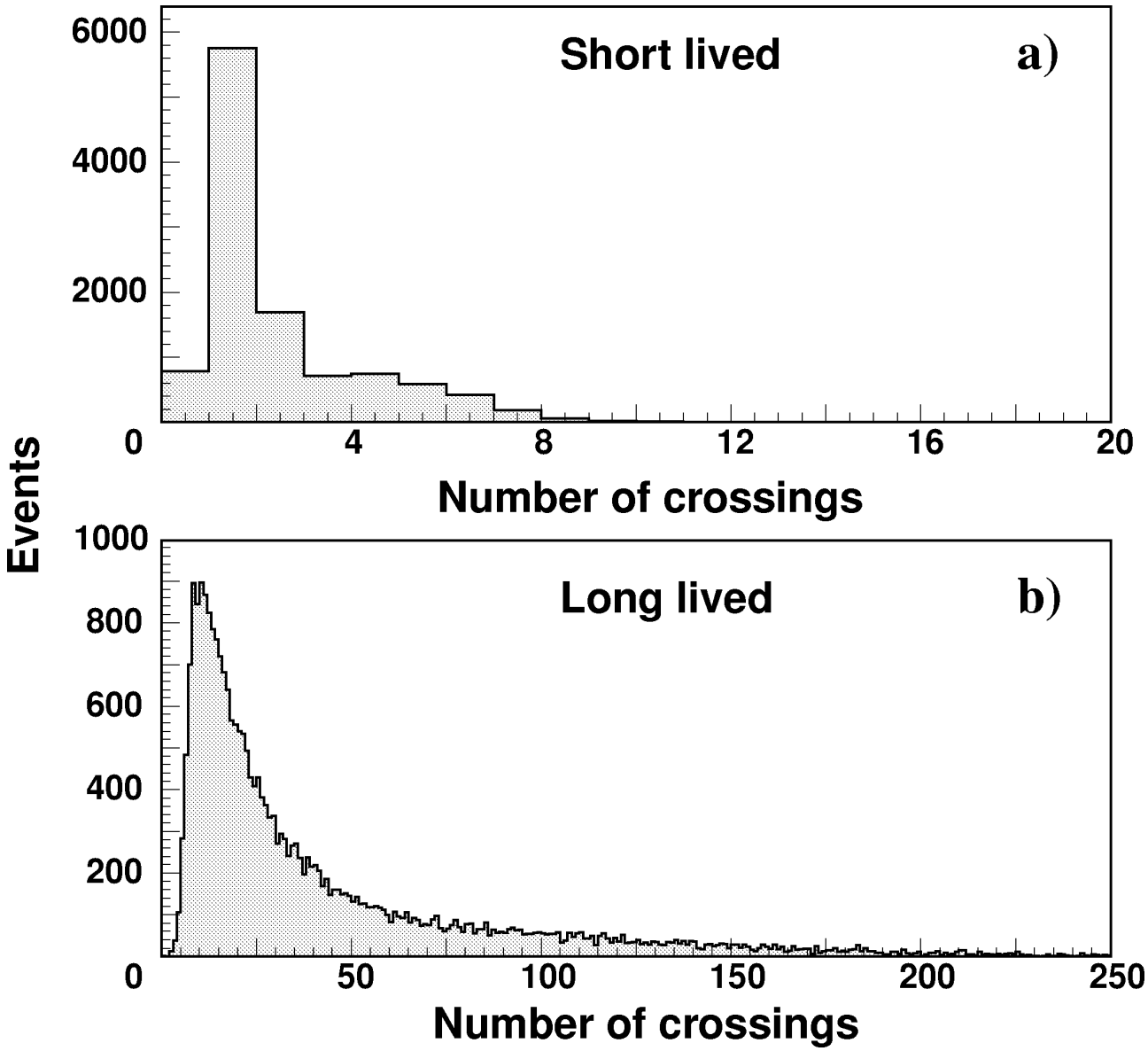

Figure 7: Number of times the back traced trajectory crosses the geomagnetic equator for a) short–lived and b) long–lived protons ($\Theta_M < 0.3, p < 3$ GeV/c).